ALMA Band 3 polarimetric follow-up of a complete sample of faint PACO sources

V. Galluzzi [1,2]★ G. Puglisi [3,4] S. Burkutean,[2] E. Liuzzo,[2] M. Bonato [2]
M. Massardi,[2]★ R. Paladino,[2] L. Gregorini,[2] R. Ricci,[2] T. Trombetti,[2,5] L. Toffolatti,[6,7]
C. Burigana,[2,8,9] A. Bonaldi [10] L. Bonavera [6] V. Casasola,[2,11] G. De Zotti,[12]
R. D. Ekers,[13,14] S. di Serego Alighieri,[11] M. López-Caniego[15] and M. Tucci[16]

[1] *INAF, Osservatorio Astronomico di Trieste, via Gian Battista Tiepolo 11, I-34143 Trieste, Italy*
[2] *INAF, Istituto di Radioastronomia, via Piero Gobetti 101, I-40129 Bologna, Italy*
[3] *SISSA, via Bonomea 265, I-34136 Trieste, Italy*
[4] *INFN-Sezione di Trieste, via Valerio 2, I-34127 Trieste, Italy*
[5] *INFN-Sezione di Ferrara, via Giuseppe Saragat 1, I-44122, Ferrara, Italy*
[6] *Departamento de Física Universidad de Oviedo, C. Federico García Lorca 18, E-33007 Oviedo, Spain*
[7] *INAF-OAS Bologna, via Piero Gobetti 93/2, I-40129 Bologna, Italy*
[8] *Dipartimento di Fisica e Scienze della Terra, Università degli Studi di Ferrara, via Giuseppe Saragat 1, I-44100 Ferrara, Italy*
[9] *INFN-Sezione di Bologna, via Irnerio 46, I-40126 Bologna, Italy*
[10] *SKA Organization, Jodrell Bank, Lower Whitington, Macclesfield SK11 9DL, UK*
[11] *INAF - Osservatorio Astrofisico di Arcetri, Largo Enrico Fermi 5, I-50125 Firenze, Italy*
[12] *INAF, Osservatorio Astronomico di Padova, Vicolo dell'Osservatorio 5, I-35122 Padova, Italy*
[13] *CSIRO Astronomy and Space Science, PO Box 76, Epping, NSW 1710, Australia*
[14] *International Centre for Radio Astronomy Research, Curtin University, Bentley, WA 6102, Australia*
[15] *European Space Agency, ESAC, Camino bajo del Castillo, s/n, Urbanización Villafranca del Castillo, Villanueva de la Cañada, E-28692 Madrid, Spain*
[16] *Département de Physique Théorique and Center for Astroparticle Physics (CAP), University of Geneva, 24 quai Ernest Ansermet, CH-1211 Geneva, Switzerland*

ABSTRACT

We present Atacama Large Millimetre/submillimiter Array (ALMA) high sensitivity ($\sigma_P \simeq$ 0.4 mJy) polarimetric observations at 97.5 GHz (Band 3) of a complete sample of 32 extragalactic radio sources drawn from the faint *Planck*–ATCA Co-eval Observations (PACO) sample ($b < -75°$, compact sources brighter than 200 mJy at 20 GHz). We achieved a detection rate of 97 per cent at 3σ (only 1 non-detection). We complement these observations with new Australia Telescope Compact Array (ATCA) data between 2.1 and 35 GHz obtained within a few months and with data published in earlier papers from our collaboration. Adding the co-eval GaLactic and Extragalactic All-sky Murchison widefield array (GLEAM) survey detections between 70 and 230 MHz for our sources, we present spectra over more than 3 decades in frequency in total intensity and over about 1.7 decades in polarization. The spectra of our sources are smooth over the whole frequency range, with no sign of dust emission from the host galaxy at mm wavelengths or of a sharp high frequency decline due, for example, to electron ageing. We do however find indications of multiple emitting components and present a classification based on the number of detected components. We analyse the polarization fraction behaviour and distributions up to 97 GHz for different source classes. Source counts in polarization are presented at 95 GHz.

Key words: galaxies: active – galaxies: statistics – radio continuum: galaxies.

★ E-mail: vincenzo.galluzzi@inaf.it (VG); massardi@ira.inaf.it (MM)

1 INTRODUCTION

The most commonly used model for the spectral energy distribution (SED) of blazars, i.e. compact, radio loud active galactic nuclei (AGNs), is a leptonic, one-zone model, where the emission originates in a single component (Böttcher 2012). The SEDs typically consist of two broad-band bumps: the one at lower frequencies is attributed to synchrotron radiation while the second, peaking at γ-ray energies, is attributed to inverse Compton.

The one-zone model is generally found to provide an adequate approximation primarily because of the limited observational characterization of the synchrotron SED, with fragmentary data over a limited frequency range. However, the synchrotron emission is originated by relativistic jets, and Very Long Baseline Interferometry (VLBI) images show multiple knots often called 'components' of the jet. The standard model interprets the knots as due to shocks that enhance the local synchrotron emission.

The spectrum is explained as the result of the superposition of different synchrotron self-absorbed components in a conical geometry (Marscher 1996). The synchrotron self-absorption optical depth scales as $\tau_{\mathrm{sync}} \propto B_\perp^{(p+2)/2} \nu^{-(p+4)/2}$, where $B_\perp$ is the magnetic field component perpendicular to the electron velocity and p is spectral index of the energy distribution of relativistic electrons (typically, $p \simeq 2.5$). Thus, τ_{sync} increases along the jet towards the nucleus as the magnetic field intensity and its ordering increases. At the same time, it is strongly frequency dependent: as the observing frequency increases, the emission becomes detectable at progressively smaller distances from the central engine.

Thus, the millimetre-wave emission provides information on the innermost regions of the jets, close to the active nucleus, where it is optically thin, while the emission at longer wavelengths is affected by self-absorption (Jorstad et al. 2007; Agudo et al. 2014). Interestingly, León-Tavares et al. (2011), Jorstad et al. (2013), and Ramakrishnan et al. (2016) found a significant correlation between simultaneous γ-ray fluxes and millimetre-wave flux densities of flat spectrum radio quasars (FSRQs), especially with high-optical polarization. The strongest γ-ray flares were found to occur during the rising/peaking stages of millimetre flares. This suggests that the γ-ray flares originate in the millimetre-wave emitting regions of these sources.

Polarization carries information on the magnetic field configuration (geometry and degree of order). In the shocked regions in the jet, the magnetic field is compressed. The compression makes it effectively more ordered, increasing the polarization degree (see e.g. Hughes, Aller & Aller 1989). Multifrequency polarimetry is therefore a key indicator of the physical conditions in a jet.

The origin of the observed strong variability in the synchrotron emission of blazars is still debated. The 'shock-in-jet' model (Hughes, Aller & Aller 1985; Marscher & Gear 1985) was shown to provide a promising framework to account for the frequency dependencies of variability amplitudes and time-scales (e.g. Fromm, Fuhrmann & Perucho 2015; Fuhrmann et al. 2016). According to this model, a shock wave propagates through a conical jet. Knots are interpreted as the bright downstream regions of such flow structure. Particles are accelerated to relativistic energies at the shock front and then loose energy via Compton scattering, synchrotron emission, and adiabatic losses. The variation of the Doppler factor along the jet has a major role in determining the frequency dependence of the variability parameters.

Polarization variability provides particularly useful clues to modelling (Hughes et al. 1989). While in the quiescent phase blazars are polarized at a few per cent level, individual knots can be highly polarized. This implies that the overall magnetic field is highly turbulent, the field in regions responsible for the outbursts is much more ordered. Hence the frequency dependence of the polarized emission is a powerful tool to identify emission regions that would be otherwise unresolved. However, evidences of multicomponent contributions to the synchrotron SED are still limited, although the situation has been improving in recent years (e.g. Planck Collaboration XV 2011; Cutini et al. 2014).

Our group has been carrying out a long-term programme of multifrequency observations with the Australia Telescope Compact Array (ATCA) of the *Planck*–ATCA Co-eval Observations (PACO) sample. The PACO project (Massardi et al. 2016, and references therein) observed 482 Australia Telescope 20 GHz survey (AT20G) extragalactic sources (at Galactic latitude $|b| > 5°$ and outside a $5°$ radius circle around the Large Magellanic Cloud). Of these, 344 objects constitute three partially overlapping sub-samples, selected for different purposes: the 'faint sample' comprises 159 sources with $S_{20\,\mathrm{GHz}} > 200$ mJy with $3\,\mathrm{h} < \mathrm{RA} < 9\,\mathrm{h}$ and $\delta < -30°$, and allowed us to characterize radio source spectra below the sensitivity of the *Planck* satellite over an area near to the southern ecliptic pole (where *Planck* sensitivity was maximal); the 'bright sample', namely the 189 sources with $S_{20\,\mathrm{GHz}} > 500$ mJy and $\delta < -30°$, and the 'spectrally selected' one, i.e. the 69 sources with $S_{20\,\mathrm{GHz}} > 200$ mJy (over the whole southern sky) classified as inverted- or upturning-spectrum by Massardi et al. (2011).

Galluzzi et al. (2018) have presented high sensitivity polarimetric observations in seven bands, from 2.1 to 38 GHz, of 104 compact extragalactic radio sources drawn from the faint PACO sub-sample, i.e. brighter than 200 mJy at 20 GHz. Combining these results with the GaLactic and Extra-galactic All-sky Murchison widefield array (GLEAM) survey data at 20 frequencies between 72 and 231 MHz (Hurley-Walker et al. 2017), it was found that about 90 per cent of their sources showed clear indications of at least two emission components. The broad frequency coverage and the polarimetry proved to be essential to reach this conclusion: total intensity data from 5.5 to 38 GHz could be interpreted in terms of a single emission component (Galluzzi et al. 2017).

In this paper, we extend the frequency coverage in total and polarized intensity of a complete sub-sample of 32 sources, drawn from the Galluzzi et al. (2018) sample, by means of high sensitivity observations with the Atacama Large Millimetre/submillimiter Array (ALMA) at 97.5 GHz (Band 3).

Apart from providing information on the physics of inner regions of relativistic jets, mm-wave polarimetric observations have two other important astrophysical applications.

Radio sources are the dominant contaminants of cosmic microwave background (CMB) maps on small scales down to mm wavelengths. An accurate characterization of their polarization properties is especially crucial for attempts to measure the primordial *B*-mode polarization down to values of the tensor to scalar ratios $r \sim 0.001$. The accurate simulations by Remazeilles et al. (2018) have shown that, at these values of r, unresolved polarized point sources can be the dominant foreground contaminant over a broad range of angular scales (multipoles $\ell \gtrsim 50$). These results have been confirmed by Puglisi et al. (2018) who exploited the state-of-the-art data sets of polarized point sources over the 1.4–217 GHz frequency range (including the distribution of polarization fractions presented in this paper), in order to forecast extragalactic radio sources contamination of the CMB B-mode angular power spectrum, with reference to some existing or planned ground-based or space-

borne CMB facilities (e.g. QUIJOTE,[1] LiteBIRD[2], and CORE[3]): since the other important point source population in the frequency range of CMB experiments, dusty galaxies, is believed to be very weakly polarized, radio sources are expected to dominate small-scale polarization fluctuations up to $\simeq 150$ GHz.

A polarimetric AGN catalogue at millimetre wavelengths is also necessary for the calibration of CMB maps. Furthermore, theoretical studies have examined the possible existence of terms in the Lagrangian density that can violate the Einstein Equivalence Principle (EEP), the Lorentz invariance or the CPT invariance (e.g. see Ni 2010). These terms would produce a rotation of the polarization angle along the propagation of the electromagnetic wave: this is the so-called Cosmic Polarization Rotation (CPR). The best upper limits on the CPR from CMB experiments and observations of astrophysical objects in optical or radio bands are around $1°$ (di Serego Alighieri 2015) and are limited by the calibration accuracy of the zero-point polarization angle. Finding bright point-like objects with at least a few per cent polarization fraction at high frequencies [where Faraday rotation (FR) is typically negligible] and with stable polarimetric properties (in particular, a constant polarization angle) at least on a few years time-scale may help in constraining this effect on a sub-degree scale. With our multifrequency and multi-epoch ATCA observations corroborated by the present ALMA follow-up at 97.5 GHz, we identify some potential candidates for CPR studies calibration.

The paper is organised as follows. In Section 2 we present the observational campaigns. In Section 3 we briefly describe the data reduction and flux density extraction. In Section 4 we discuss the data analysis, the spectral behaviour, and the polarimetric properties of sources. In Section 5 we present the source counts in polarized flux density at 95 GHz obtained by convolving the total intensity differential source counts with the observed polarization fraction distribution. In Section 6 we discuss peculiar objects, such as the Fanaroff–Riley Class II (FR-II) object AT20G0408-750528 and the blazar PKS0521−365 (our leakage calibrator), for which a more extended multifrequency and multi-epoch investigation at VLBI resolution will be presented in a forthcoming paper (Liuzzo et al., in preparation). We also identify some potential CPR calibrators. Finally, in Section 7 we draw our conclusions.

2 ALMA OBSERVATIONS

The observations were carried out with ALMA (Cycle 3, Project ID: 2015.1.01522.S, PI: Galluzzi) on 2016 August 24, and September 22th and 27th, in four 2 GHz-wide spectral bands centred at 90.5, 92.5, 102.5, and 104.5 GHz, respectively, using 39 antennas in a compact configuration (baseline range 118–1318 m, corresponding to resolutions of 4.8–0.3 arcsec at 97.5 GHz).

We observed a complete sample of 32 objects drawn from the faint PACO sample ($S_{20\,\mathrm{GHz}} > 200$mJy) in three circular regions at $b < -75°$ (each with $\sim 10°$ diameter) that, altogether, contain $\simeq 60$ per cent of the 53 sources observed by Galluzzi et al. (2017). The three regions were selected in order to optimize the use of ALMA time, maximizing the sample size with the smallest possible number of science goals (SGs; see Fig. 1), where the term 'SG' indicates a small group of sources which share the same spectral
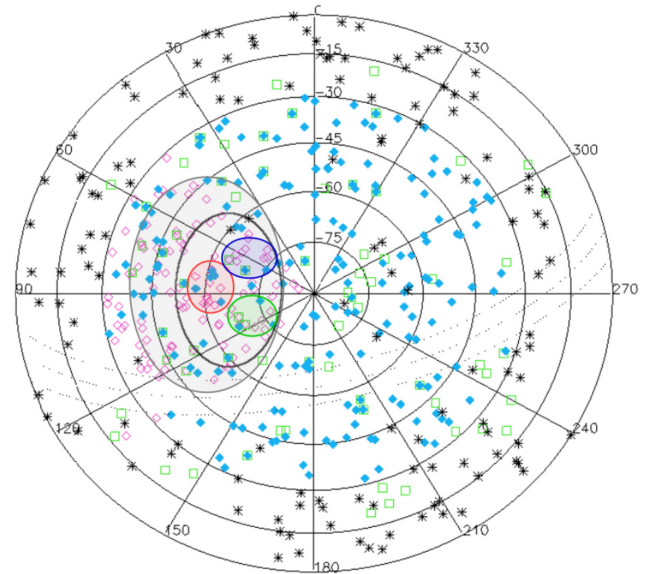
Figure 1. Polar equal-area projection map showing the positions of PACO sources (RA and Dec. are in degrees). The faint PACO sources are shown as open pink diamonds, the bright PACO ones as filled blue diamonds. Green squares are for the spectrally selected PACO sample and black asterisks are for blazars and Australia Telescope (AT) calibrators, respectively. The dotted lines indicate the Galactic plane and mark the area with Galactic latitude $|b| < 5°$ (cf. Massardi et al. 2016). The black and the grey ellipses enclose the samples investigated by Galluzzi et al. (2017, 2018), respectively. The smaller red, green, and blue ellipses encircle the three SGs of ALMA observations.

and sensitivity requirements, and the same calibration. The latter requires at least 3 h of observations for each polarimetric SG, in which observations of the target are interleaved with those of the polarization calibrator, to achieve the adequate parallactic angle coverage for the computation of polarimetric 'leakage' (D-terms).

This allowed us to get in linear polarization a 3σ detection rate of 97 per cent (only one non-detection) and a 5σ detection rate of $\simeq 94$ per cent (only two non-detections). The median significance of detections is $\simeq 10\sigma$.

The sources were unresolved by ATCA at all frequencies (up to 38 GHz). Our ALMA observations achieved a resolution of $\simeq 0.2$ arcsec, a factor $\simeq 25$ higher than that of ATCA observations at 38 GHz. The possibility that some sources might be resolved by ALMA was considered in our flux density estimation approach and in some of the analyses described in the following sections.

3 DATA REDUCTION

ALMA data were calibrated by using the Common Astronomical Software Applications (CASA) version 4.7.0, following the current standard calibration scheme reported in Nagai et al. (2016) and the CASA guide.[4] In Table 1 we report the list of the calibrators visited during the ALMA observations. The ALMA data reduction consists of two steps: the first one corrects only the parallel hands products, i.e. XX and YY and the second one (needed in case of polarimetry) addresses the cross products XY and YX, and the refinement of XX and YY gains.

---

[1]Q-U-I JOint TEnerife.
[2]Lite satellite for the studies of B-mode polarization and Inflation from cosmic background radiation detection.
[3]Cosmic ORigin Explorer.

[4]https://casaguides.nrao.edu/index.php/Main_Page

Table 1. List of the calibrators visited during our ALMA observations. The second column reports the SG observed in a given epoch.

Epoch	SG	Bandpass	Flux	Phase	Leakage
24/08/16	1	J0635−7516	J0519−4546	J0715−6829	J0538−4405
22/09/16	3	J0635−7516	J0519−4546	J0440−6952	J0522−3627
27/09/16	2	J0635−7516	J0519−4546	J0715−6829	J0538−4405

Table 2. ALMA array configuration, minimum and maximum angular scales, time on source and sensitivity for each SG of our observations.

SG	Array conf.	Min.–max. scale (arcsec)	Time on source (min)	Sens. (μJy)
1	C40-6	0.4–4.8	5.04	40
3	C40-6	0.2–4.8	11.69	20
2	C40-6	0.2–4.8	11.69	20

Since almost all the objects are point-like, *I*, *Q*, and *U* Stokes flux densities are extracted from the corresponding maps (obtained with a natural weighting) by modelling the emission with a 2D Gaussian (whose widths are of the order of the FWHM of the synthesized beam, i.e. 0.3 arcsec) and deriving the integrated flux densities. Whenever the fit fails because the source is too faint to be detected in Stokes *Q* and *U*, we consider the central peak in the image. The flux density extraction for resolved objects is addressed in Section 6.

In the Table 2 we report details about the array configuration, the minimum and maximum angular scales, the time on source and the sensitivity achieved for each SG.

During ALMA Cycle 3 Stokes *V* (circular polarization) was still under commissioning. Stokes *V* images obtained were not reliable, hence, differently from our previous works (Galluzzi et al. 2017, 2018), we cannot use the first-order debiasing technique. However, our experience with high sensitivity (0.6 mJy) ATCA data have shown that the debiasing term σ_V lowers the estimated value of the polarized flux density by ~ 0.01 per cent, well within our assumed calibration error (~ 10 per cent). Hence, the linearly polarized emission, *P*, can be safely estimated from the Stokes parameters *Q* and *U* only

$$P = \sqrt{Q^2 + U^2}. \tag{1}$$

The polarization angle ϕ and the polarization fraction Π (usually in terms of a percentage) write

$$\phi = \frac{1}{2} \arctan\left(\frac{U}{Q}\right), \tag{2}$$

$$\Pi = 100 \times P/I. \tag{3}$$

The errors in total intensity, linear polarization flux density, and position angle were computed as in Galluzzi et al. (2017), i.e. adopting calibration errors added in quadrature to the statistical ones. The CASA guide recommends to use a 10 per cent of the measured flux density for Stokes' *I*, *Q*, and *U* and an additional $2°$ for the instrumental error on the polarization angle. Indeed we assumed a lower error for *I* (i.e. 7 per cent) because the primary calibrator, namely the core of Pictor A (AT20GJ051949−454643), is found to be stable within ~ 2 per cent both at 91.5 and 103.5 GHz during the one month period before and after our observations.

All the flux densities (total intensity and polarization), the polarization angle, and the polarization fractions are reported in Table 3.

4 DATA ANALYSIS

We adopted a 3σ limit for detections in polarization. The median sensitivity in polarization for our ALMA observations (including the calibration error), is $\simeq 0.4$ mJy. We achieved a detection rate of $\simeq 97$ per cent: only 1 object is non-detected, AT20GJ054641−641522. This is a quasar that went undetected in polarization also by our ATCA observations in both the 2014 and the 2016 campaigns, with 5σ detection limits in the 33–38 GHz band of 0.7 and 2 mJy, respectively.

In the following sub-sections we discuss the polarimetric properties of our sample, combining observations from 2 GHz (epoch: 2016 March and April, Galluzzi et al. 2018), through the 5.5–38 GHz range (epochs: 2014 September, 2016 March and April, presented in Galluzzi et al. (2017, 2018), and new observations of 2016 July) and up to 104.5 GHz (ALMA observations, 2016 August and September). In the analysis of total intensity spectra we include GLEAM data. We exclude from the analysis the FR-II source AT20GJ040848−750720, which was resolved by ALMA. ALMA observations of this source are presented in Section 6.

4.1 Spectral behaviour

The ATCA and ALMA observations are not simultaneous. While ALMA observations were carried out at the end of August and at the end of 2016 September, ATCA observations at 33–38 GHz were performed at the beginning of 2016 April for half of this sample, and at mid July 2016 for the other half. The whole sample of 32 objects was observed at 2.1 and 5.5–9 GHz in 2016 March and April, and only 13 objects have measurements repeated in July.

At frequencies higher than 20 GHz, variability frequently exceeds 10 per cent even on time-scales of few months. Therefore we have not attempted a joint fit of ALMA and ATCA data, also on account of the ~ 50 GHz frequency gap between the two data sets.

Fig. 2 shows, for each source in our sample, a collection of total intensity and polarization measurements. At the bottom of each panel, we also display a plot of the linear polarization fractions and, below each panel, a plot of the position angles as a function of frequency. Together to ALMA data, we display measurements collected during ATCA 2014 and 2016 observations. Moreover, in total intensity we include GLEAM (Hurley-Walker et al. 2017), the Sydney University Molonglo Sky Survey (SUMSS; Mauch et al. 2003), and PACO (Massardi et al. 2016) flux densities.

The ALMA total intensity flux densities of most (26 out of 32) sources are somewhat in excess of expectations based on fits of the ATCA 2016 total intensity measurements. The median excess is of ~ 46 per cent (with a maximum of $\simeq 98$ per cent). The polarization fraction however indicates that we are still dealing with synchrotron emission from the active nucleus. The unpolarized free–free and the weakly polarized dust emission associated with star formation in the host galaxies are expected to be much fainter. The excess is thus suggestive of a different component coming out at a few mm wavelengths.

For three sources (namely, AT20GJ035547–664533, AT20GJ053435–610606, and AT20GJ055009–573224) the absolute value of the flux density difference is less than 10 per cent, and may be accounted for by variability and/or measurement errors. Again, only three objects, namely AT20GJ050754–

Table 3. ALMA Band 3 (central frequency: 97.5 GHz) observations performed at the end of august and at the end of 2016 September. The table below reports: the sequential number, the AT20G name, the GLEAM counterpart, RA (in hours) and Dec. (in degrees), an extension flag ('.' for 'point-like', 'e' for 'extended in this observation' and 'pe' for 'probably extended'), the flux density in total intensity (Stokes' I), the linearly polarized flux density (P), the linear polarization fraction (Π), the polarization angle (ϕ), and associated errors for all these quantities ('<' marks a 3σ upper limit, while '-' stands for not available data). Note that we do not catalogue polarization values for the object AT20GJ040848−750720, since it is well resolved in three linearly polarized components (cf. Fig. 10). A machine-readable version of this catalogue is available as online supplementary material.

No	(AT20G) name	(GLEAM) name	RA (h)	Dec. (°)	Flag	I (mJy)	err$_I$	P (mJy)	err$_P$	Π (per cent)	err$_\Pi$	ϕ (°)	err$_\phi$
1	J032404−732047	J032400−732039	3.401 1192	− 73.346 3898	.	63.42	4.44	1.90	0.19	3.00	0.37	-	-
2	J033243−724904	J033242−724906	3.545 3087	− 72.818 0313	.	75.48	5.29	1.29	0.13	1.71	0.21	3.6	2.2
3	J034028−670316	J034028−670315	3.674 4947	− 67.054 6722	.	145.54	10.19	0.66	0.08	0.45	0.06	− 38.0	3.1
4	J035547−664533	J035548−664532	3.929 9614	− 66.759 3613	.	241.01	16.88	1.93	0.17	0.80	0.09	− 57.1	2.6
5	J040820−654508	J040820−654458	4.139 0414	− 65.752 2812	pe	24.28	1.70	2.11	0.16	8.69	0.90	− 63.2	2.8
6	J040848−750720	J040848−750716	4.146 8747	− 75.122 2534	e	106.55	7.46	-	-	-	-	-	-
7	J042506−664650	J042507−664656	4.418 5832	− 66.780 5786	.	33.24	2.33	0.83	0.07	2.51	0.28	− 67.0	3.2
8	J044047−695217	-	4.679 9779	− 69.871 5286	.	307.31	21.52	11.12	1.11	3.62	0.44	92.5	2.0
9	J050644−610941	J050643−610941	5.112 2279	− 61.161 4990	pe	370.48	25.95	5.38	0.53	1.45	0.18	94.3	2.1
10	J050754−610442	J050754−610443	5.131 8527	− 61.078 5789	.	273.49	19.16	13.59	0.99	4.97	0.50	64.4	2.8
11	J051637−723707	-	5.277 2115	− 72.618 8278	.	204.64	14.33	6.94	0.53	3.39	0.35	16.7	2.7
12	J051644−620706	J051644−620702	5.279 1331	− 62.118 3586	.	653.56	45.79	24.77	1.76	3.79	0.38	− 24.1	2.8
13	J052234−610757	J052233−610800	5.376 2222	− 61.132 4997	.	146.58	10.27	0.97	0.10	0.66	0.08	29.2	3.4
14	J053435−610606	J053435−610605	5.576 5971	− 61.101 9211	.	170.48	11.94	5.47	0.49	3.21	0.37	35.2	2.4
15	J054641−641522	J054642−641513	5.778 2806	− 64.256 1417	.	20.36	1.43	<0.18	0.06	<0.91	0.30	-	-
16	J055009−573224	J055009−573226	5.835 9914	− 57.540 1688	.	814.86	57.09	60.62	5.25	7.44	0.83	33.7	2.5
17	J060755−603152	J060755−603154	6.132 0002	− 60.531 1699	.	244.42	17.12	3.83	0.37	1.57	0.19	− 38.8	2.2
18	J061030−605838	J061030−605841	6.175 0778	− 60.977 3293	.	81.64	5.72	1.54	0.16	1.88	0.24	-	-
19	J062005−610732	J062004−610737	6.334 7946	− 61.125 6409	.	120.89	8.47	12.65	0.92	10.46	1.05	70.4	2.8
20	J062153−593509	J062153−593510	6.364 7527	− 59.585 9718	.	89.93	6.30	0.43	0.08	0.48	0.09	− 20.2	5.4
21	J062307−643620	J062307−643624	6.385 4808	− 64.605 7205	.	285.89	20.03	10.81	1.02	3.78	0.44	− 7.2	2.2
22	J062524−602030	J062523−602025	6.423 4222	− 60.341 6901	.	81.30	5.70	0.23	0.07	0.28	0.09	-	-
23	J062857−624845	J062857−624851	6.482 6421	− 62.812 5610	.	222.78	15.62	4.41	0.33	1.98	0.20	− 70.4	2.9
24	J063546−751616	J063547−751617	6.596 2026	− 75.271 3318	pe	1199.43	83.99	18.86	1.60	1.57	0.17	− 12.2	2.5
25	J064428−671257	J064428−671253	6.741 1112	− 67.216 0568	.	410.77	28.77	4.78	0.48	1.16	0.14	− 1.8	2.0
26	J070031−661045	J070031−661043	7.008 6578	− 66.179 1916	.	599.90	42.01	22.92	2.28	3.82	0.47	88.3	2.0
27	J071509−682957	J071511−683010	7.252 6306	− 68.499 3134	.	168.92	11.83	4.06	0.40	2.41	0.29	41.8	2.1
28	J073856−673551	J073856−673550	7.648 9721	− 67.597 5037	.	99.07	6.94	1.85	0.18	1.86	0.23	49.8	2.2
29	J074331−672625	J074332−672628	7.725 4445	− 67.440 4678	pe	198.09	13.88	10.26	1.03	5.18	0.63	1.0	2.0
30	J074420−691906	J074421−691908	7.738 9582	− 69.318 4662	.	155.15	10.87	15.22	1.22	9.81	1.04	59.6	2.6
31	J075714−735308	J075714−735306	7.953 9001	− 73.885 7498	.	58.83	4.12	2.00	0.20	3.40	0.42	-	-
32	J080633−711217	J080632−711215	8.109 4167	− 71.204 7501	pe	84.07	5.89	0.33	0.05	0.40	0.06	− 66.9	4.5

610442, AT20GJ051644−620706, and AT20GJ062307−643620, have ALMA flux densities significantly fainter than expected. The deficits are of $\simeq$ 10 per cent, 18 per cent, and 81 per cent, respectively. However, even in the latter case there is no sign of a spectral break and the median spectral index in total intensity between 36.5 and 97.5 GHz is $\alpha_{36.5}^{97.5} \simeq -0.19$ (we use the convention $S_\nu \propto \nu^\alpha$). This result is in very good agreement with the predictions of the C2Co model (Tucci et al. 2011, see their Table 6), albeit in a slightly different frequency interval, namely 30–100 GHz.

Fig. 3 compares the spectral indices in total intensity and in polarization between 36.5 (the central frequency of ATCA 2016 observations) and 97.5 GHz (the central frequency of ALMA observations). Total intensity spectral indices, $\alpha_{36.5}^{97.5}$, are, with a few exceptions, in the range −0.50–0.50. In polarization there are a couple of sources with spectral indices, $\alpha_{p,36.5}^{97.5}$ as steep as −1.5 or even −2.0.

There are also two sources with $\alpha_{p,36.5}^{97.5} \geq 1$ and seven sources undetected in polarization at 35 or 38 GHz but detected at 97.5 GHz, i.e. with only a lower limit to $\alpha_{p,36.5}^{97.5}$. Only part of these lower limits may be understood in terms of the higher sensitivity of ALMA

observations compared to the ATCA ones. In other cases they provide further support to indications of an additional synchrotron component showing up at frequencies of $\sim$ 200–300 GHz in the source frame.
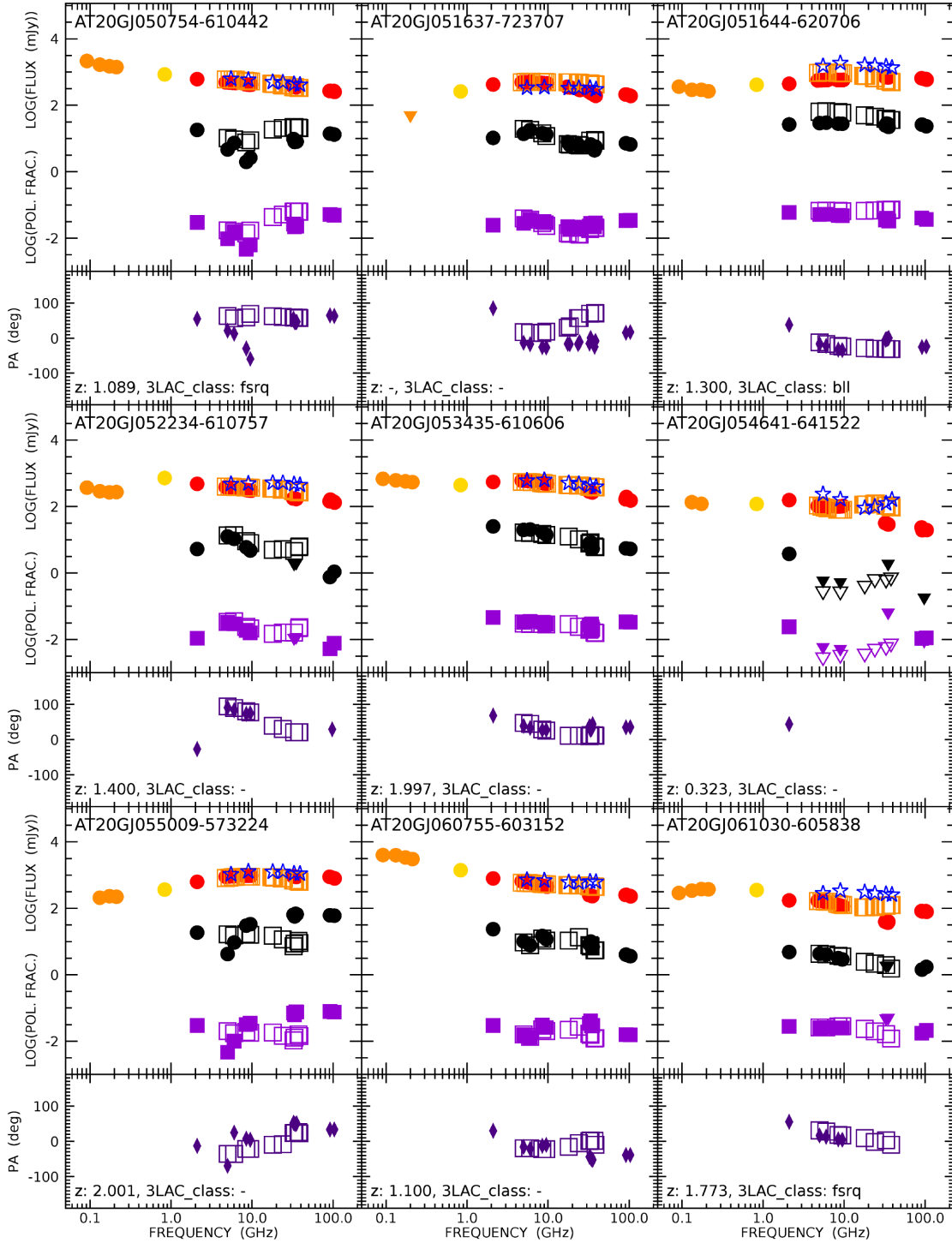
4.2 Linear polarization fraction

The median polarization fraction measured by ALMA for the full sample is 2.2 ± 0.6 per cent, close to the median value at 38 GHz (2.09 per cent) for the larger sample of 104 objects (cf. Galluzzi et al. 2018). Our result is in good agreement with estimates based on *Planck* maps at 100 GHz obtained by applying stacking techniques by Bonavera et al. (2017, 1.8 (+0.4, −0.3) per cent) and by using intensity distribution analysis (IDA) method by Trombetti et al. (2018, 1.8 ± 0.5 per cent).

We also estimated the distribution of the percentage polarization fraction, Π, using a bootstrap and re-sampling approach. Each detection was associated with the mean value of a Gaussian with σ given by the error on the polarization fraction. When only an upper limit is available, we used a uniform distribution between 0 and the 3σ upper limit. Then, we generated 1000 simulated data
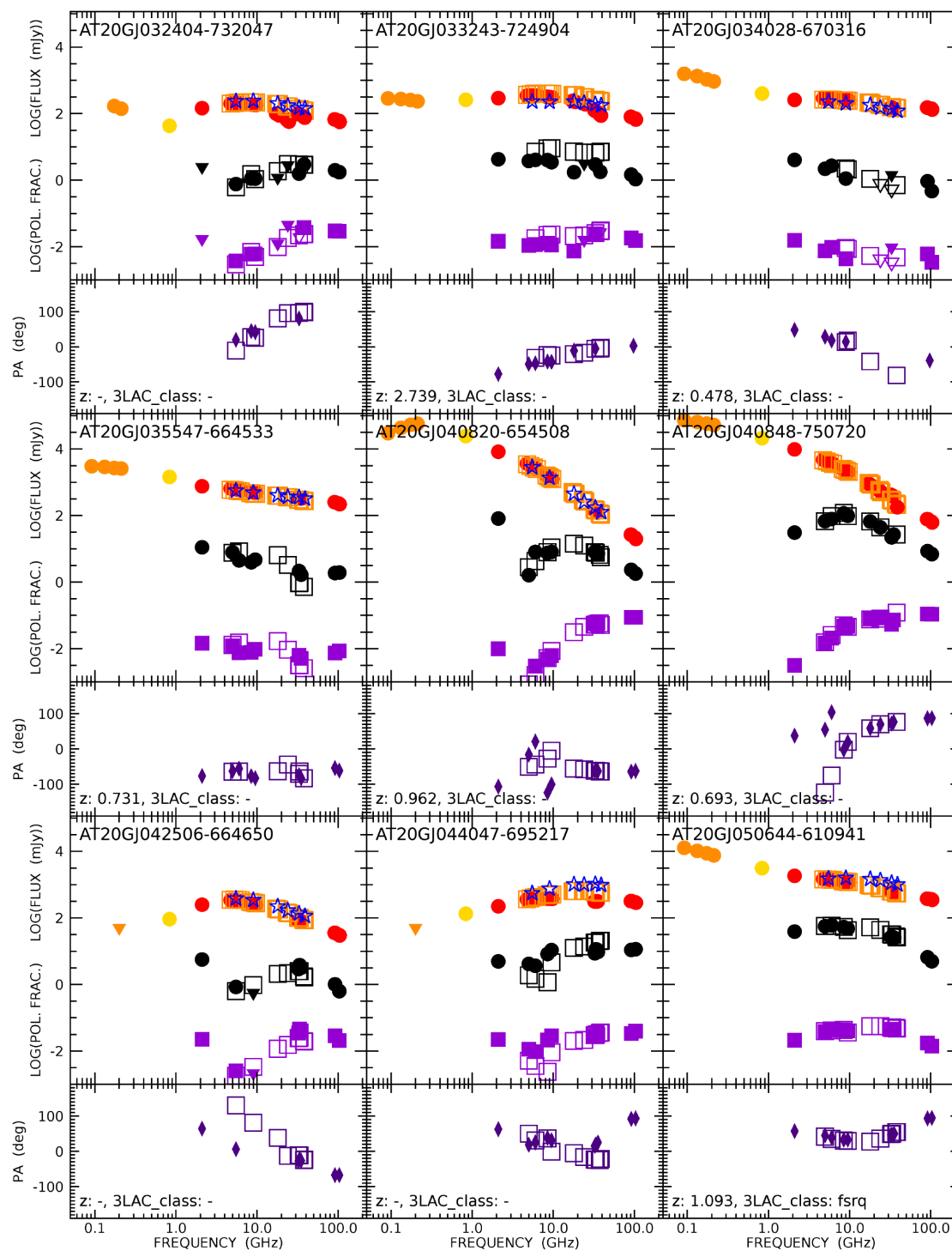
Figure 2. Spectra in total intensity, in polarization, in polarization fraction, and in polarization angle for the 32 objects of the faint PACO sample, observed with ALMA. The error bars are not displayed since they are smaller than the symbols. *Total intensity*: filled red circles indicate ATCA 2016 and ALMA observations. The filled orange and yellow circles show GLEAM and SUMSS flux densities, respectively. The orange squares are ATCA 2014 observations and the blue stars are PACO observations (2009, 2010). *Polarization (flux density)*: filled black circles refer to ATCA 2016 and ALMA observations. Upper limits are shown as black filled downwards-pointing triangles. Black squares represent previous ATCA observations (2014 September). Their upper limits are displayed as downwards-pointing empty black triangles. *Linear polarization fractions*: filled purple squares, with upper limits shown as downwards-pointing filled triangles, for ALMA and ATCA observations; purple squares with upper limits shown as downwards-pointing empty purple triangles for 2014 September ATCA observations. *Polarization angle*: filled indigo diamonds for ATCA 2016 and ALMA observations; indigo squares for 2014 September ATCA observations. For each object (where available) we also report the redshift z and the classification provided by the third catalogue of AGN (3LAC) released by the Fermi Collaboration (Ackermann et al. 2015).

Figure 2 – *continued.*

sets by re-sampling with repetitions the distributions of percentage polarization fractions of each source. The results of the simulation are reported in Fig. 4 and in Table 4. In Fig. 4 we also show the best-fitting lognormal function

$$\mathcal{P}(\Pi) = \frac{A}{\Pi \sigma \sqrt{2\pi}} \exp\left[-\frac{\ln^2(\Pi/\mu)}{2\sigma^2}\right], \qquad (4)$$

with $A = 0.86$, $\mu = 2.05$, and $\sigma = 0.97$.

In Galluzzi et al. (2018) we briefly discussed the spectral classification in the presence of a wide frequency coverage both in total intensity and polarization. For every object (in our sample of 104 compact extragalactic sources) we compared the spectrum in total intensity with that in linear polarization, finding in more than 90 per cent of cases signs of 2–3 synchrotron components (e.g. multiple bumps in the spectra or features appearing only in polarization, where total intensity still looks smooth). Thus, we
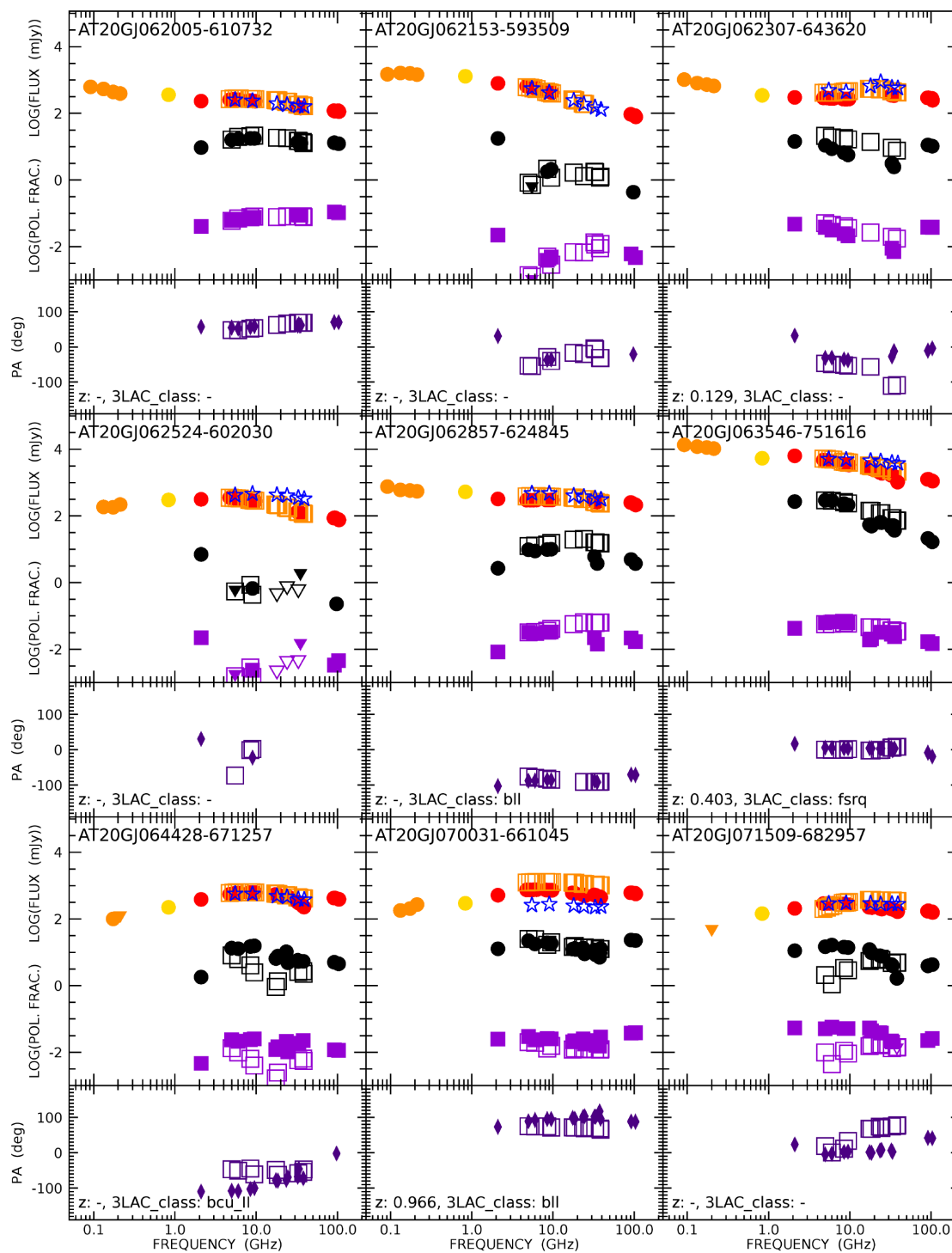
Figure 2 – *continued.*

classified objects which can be explained in terms of a single emitting region as '1C', those with 2 or 3 components as '2–3C', and sources with indications of more than three components (typically in the range 70 MHz to ∼ 30 GHz) as '> 3C'.

Here we complement the analysis about the frequency dependence of the median polarization fraction provided by Galluzzi et al. (2018) by investigating this aspect at higher frequencies (i.e. 97.5 GHz). We again apply the same classification in terms

of synchrotron components in order to distinguish between subpopulations. However, we warn the reader that this classification is based on polarimetric data collected in the 2014 campaign of ATCA observations. We were not able to update this because of the lack of 18–24 GHz polarimetric observations for several objects in 2016 campaigns and because ALMA observations are not strictly co-eval to 2016 ATCA ones (variability might bias the classification). Our sample of 32 objects displays 27 sources classified as 2–3C and 5
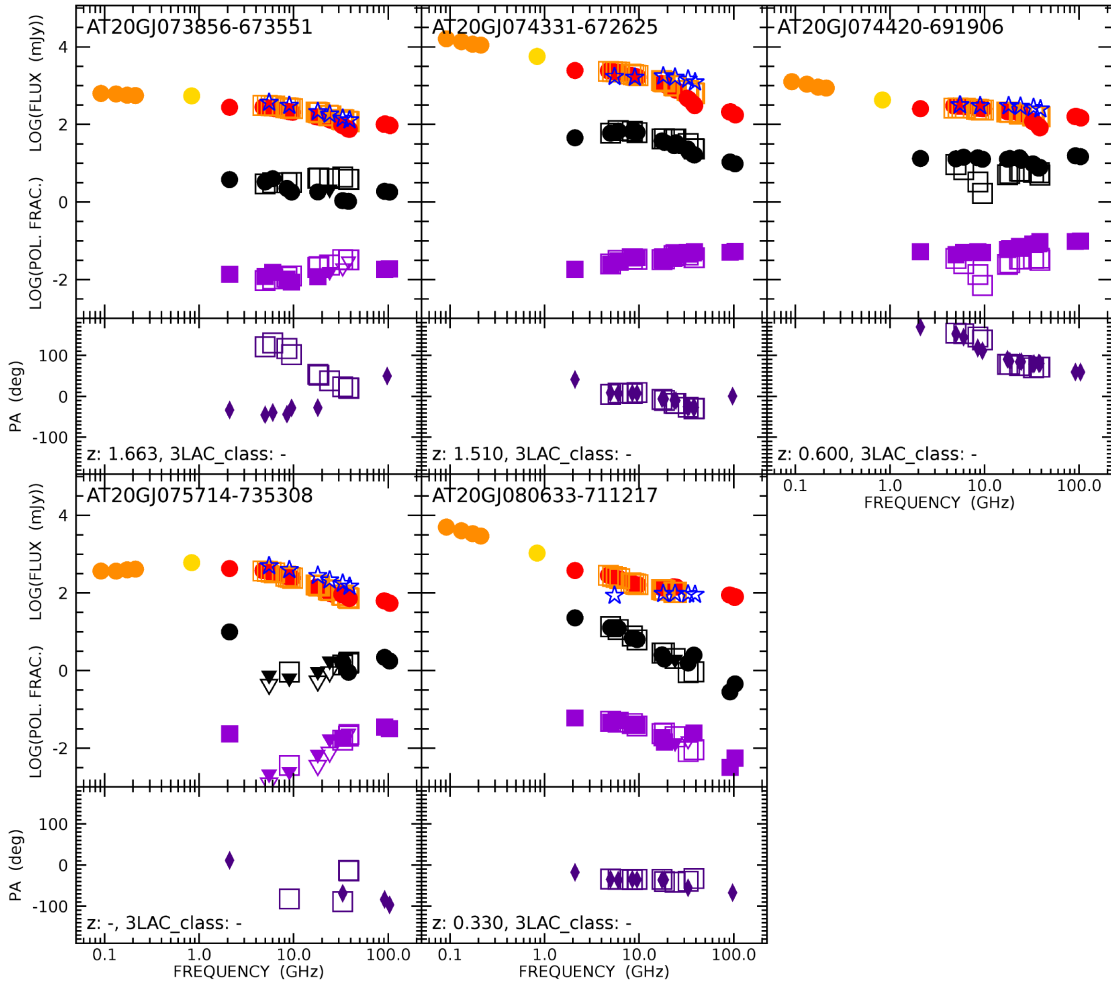
Figure 2 – *continued.*
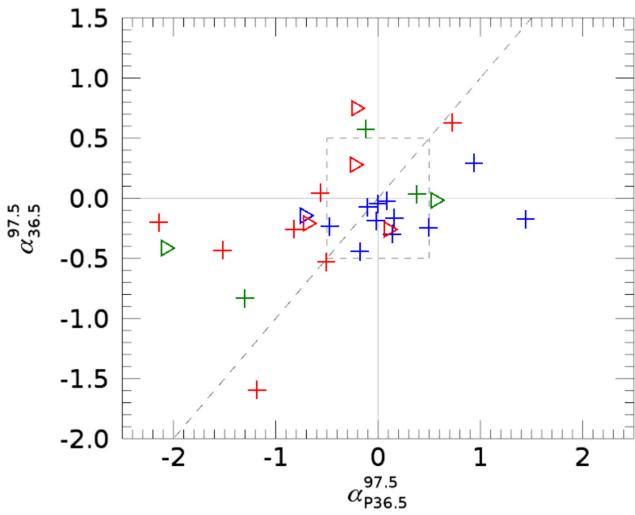
Figure 3. Colour–colour plot showing spectral indices in total intensity versus those in polarization. Different colours refer to different sub-classes in total intensity: red for steep-, green for peaked-, and blue for flat-spectrum objects (cf. the classification introduced by Galluzzi et al. 2018). Rightward-pointing triangles are for lower limits for spectral indices in polarization (non-detections at ATCA frequencies). The central square delimited by dashed lines represents the region in which both spectral indices are between −0.5 and 0.5. The other dashed line is a bisector.
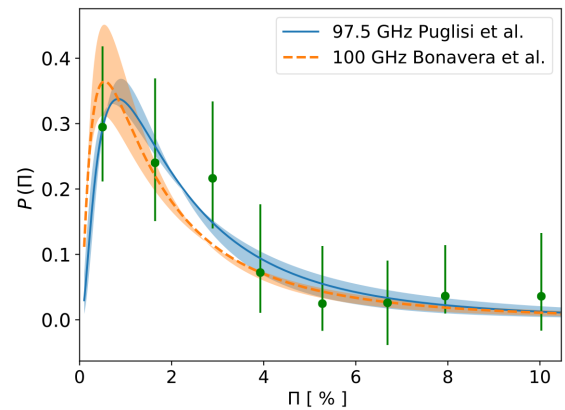
Figure 4. Distribution of the percentage polarization fraction at 97.5 GHz obtained with a bootstrap and re-sampling of the observed distribution of the polarization fractions (green points). The lognormal fit is shown by the blue solid line (the shaded area represents the 1σ uncertainty in the fitting curve, already presented by Puglisi et al. 2018). We also plot the distribution obtained by Bonavera et al. (2017, the orange dashed line with the corresponding 1σ shaded area).
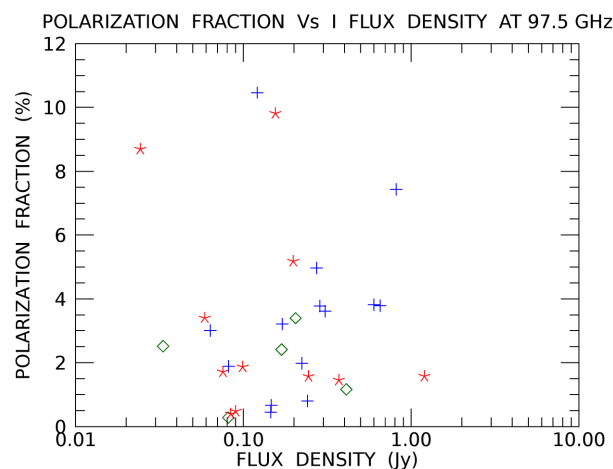
Table 4. Distribution of the percentage polarization fractions at 97.5 GHz outcoming from the bootstrap and re-sampling performed on the ALMA data.

Π (per cent)	Probability	Lower error	Upper error
0.502	0.299	0.083	0.123
1.634	0.235	0.089	0.129
2.897	0.216	0.077	0.118
3.943	0.074	0.062	0.104
5.269	0.026	0.042	0.088
6.667	0.024	0.064	0.065
7.960	0.036	0.027	0.078
10.044	0.037	0.053	0.097

Figure 6. Polarization fraction against total flux density at 97.5 GHz for the complete sample observed with ALMA. Red stars, green diamonds, and blue pluses stand for steep-, peaked-, and flat-spectrum objects, respectively (cf. Galluzzi et al. 2018).

where rms is the standard deviation around the mean and N is the number of objects (cf. Arkin & Colton 1970). The error bars at 97.5 GHz are larger since the size of the sample is smaller by a factor ~ 3 with respect to lower frequencies.

As illustrated by the Fig. 5, the data do not indicate any statistically significant trend with frequency for all the objects. According to the analyses by Bonavera et al. (2017) and Trombetti et al. (2018), the median polarization fraction remains essentially frequency independent over the full range of *Planck* polarization measurements (30–353 GHz). Moreover, negligible frequency dependency has been found by Puglisi et al. (2018) by combining data in a wide range of frequencies (from 1.4 to 217 GHz).

As pointed out by Galluzzi et al. (2018), sources with 2–3 spectral components (2–3C) seem to show a minimum of the polarization fraction at ~ 10 GHz while for sources with more than 3 components (> 3C) a slight decrease above this frequency is indicated by the data. The ALMA measurements are consistent (although with large uncertainties) with frequency independent polarization fractions above some tens of GHz.

Trombetti et al. (2018) also found no evidence of a dependence of the median polarization fraction on the total flux density. As shown by Fig. 6 the ALMA data are consistent with this result: there is no sign of a correlation between the polarization fraction and the total flux density, neither for the full sample nor for steep-, peaked-, and flat-spectrum objects (identified by red stars, green diamonds, and blue pluses, respectively) separately. However, the small size of the sample prevents any firm conclusion.

Figure 5. Frequency dependence of the median polarization fraction for sources with different spectral classification. At 2.1, 5.5, 9, 18, 24, 33, and 38 GHz we show the median polarization percentages, with their uncertainties, for the larger sample studied by Galluzzi et al. (2018), comprising a total of 104 sources. To these estimates we have added the median polarization percentage at 97.5 GHz for the complete sub-sample of 32 objects observed with ALMA. We also subdivide the sources by the number of spectral components: 1 (1C), 2–3 (2–3C), and more (> 3C).

4.3 Rotation measures at ALMA frequencies

The sensitivity of our ALMA observations has allowed several detections in Stokes Q and U with signal-to-noise ratios up to ~ 10 combining the four 2 GHz bands. For 22 objects out of 32 both Q and U were detected at a $\geq 6\sigma$ level, which in principle might allow us to have a 3σ detection in each band. Three well-determined polarization angles are the minimum requirement to study the rotation measures (RMs) of our sources. We have also attempted to split each band into two 1 GHz sub-bands, bringing to 8 the maximum number of spectral measurements per source.

sources in the > 3C class. We found no 1C objects. The results are presented in Fig. 5. The median polarization percentages at 2.1, 5.5, 9, 18, 24, 33, and 38 GHz refer to the larger sample analysed by Galluzzi et al. (2018), comprising a total of 104 sources. The median polarization percentage at 97.5 GHz is for the ALMA sample of 32 objects. The errors on median values are given by $1.253\,\mathrm{rms}/\sqrt{N}$,

In the case of a foreground screen of magnetized plasma the polarization angle varies as $\Delta\phi = RM\lambda^2$. The RMs were estimated using this relation.

Following Galluzzi et al. (2018) we used the IDL LINFIT procedure, accepting only fits with a reduced $\chi^2 < 2$ and with a probability level >0.1. In Fig. 7 we show the 19 successful fits. As discussed in Galluzzi et al. (2018) the $1/\lambda^2$ contribution to the uncertainty makes RM measurements extremely difficult at high frequencies. In our case only 11 objects have RMs not compatible with 0, at a $\geq 1\sigma$ level. In the Table 5 we report the list of the observed RMs with the associated errors provided by the fitting procedures. The median relative error for these cases is ~ 60 per cent but we warn the reader that in four cases (i.e. AT20GJ050644−610941, AT20GJ050754−610442, AT20GJ051637−723707, and AT20GJ051644−620706) relative errors on RMs are as high as 80–90 per cent.

In the upper part of Table 6 we report the median values of the non-zero RMs derived from the above equation for these 11 objects. For the 7 objects with measured redshift we have computed the RMs at the source, correcting for the effect of redshift and for the relatively small contributions of our own Galaxy and of Earth's ionosphere, as detailed by Galluzzi et al. (2018); the results are given in the lower part of the table. Also shown in the table are the results for the 2–3C and the > 3C sources considered separately (there are no 1C objects in the ALMA sample).

Although the number of objects is too small to reach any firm conclusion, we note that the median RM at the source ($\simeq 6.4 \times 10^4$ rad m^{-2}) is one order of magnitude higher than that obtained for the 18–38 GHz frequency range and two orders of magnitude higher than that found for the 2–9 GHz range (cf. Galluzzi et al. 2018, their Table 4).

Our results seem to be still consistent with the indication of an increase of the median RM with increasing number of spectral components, reported by Galluzzi et al. (2018). If confirmed, the extreme values derived from ALMA measurements would require very dense screens of magnetized plasma (cf. Hovatta et al. 2019). Such screens may heavily depolarize the radiation emitted at the basis of the relativistic jet and thus offer an explanation for the lack of an observed increase of the polarization fraction with increasing frequency. In fact, the emission at higher and higher frequency is expected to come from regions closer and closer to the nucleus where the magnetic field should be more ordered and the polarization fraction correspondingly higher.

5 SOURCE COUNTS

We have exploited our ALMA polarization measurements to derive the differential source counts in polarization at 95 GHz, $n(P) \equiv \mathrm{d}N/\mathrm{d}P$. We started from the C2Ex model for total intensity source counts, $n(S)$, by Tucci et al. (2011) and used the approach of Tucci & Toffolatti (2012)

$$n(P) = \int_{S_0=P}^{\infty} \mathcal{P}\left(m = \frac{P}{S}\right) n(S)\frac{\mathrm{d}S}{S}, \tag{5}$$

where $\mathcal{P}$ is the probability density distribution for the polarization fraction $m = \Pi/100$, given by equation (4). The integration over S is truncated at $S_0 = P$, where the polarization fraction is 100 per cent; however, the result is insensitive to the choice of S_0 (provided that it is not much larger than P), since equation (4) goes rapidly to zero for $\Pi > 10$ per cent.

The Euclidean-normalized differential source counts in polarized flux density derived from equation (5) down to $\simeq 1$ mJy

(approximately the 3σ detection limit of our ALMA observations) are shown in Fig. 8 (triangles) and listed in Table 7. Given the relative smallness of the sample we have not distinguished among the sub-populations considered by the Tucci & Toffolatti (2012) model (FSRQs, BL Lacs and steep-spectrum radio sources, i.e. SSRSs): the distribution of equation (4) was applied to all sub-populations. The error bar estimation of each data point takes into account the Poissonian contribution (cf. Gehrels 1986) and the uncertainties on the parameters of the lognormal distribution. To evaluate this contribution we use the semidispersion in the polarization number counts resulting from the convolution with the maximum and minimum lognormal fitting curves, respectively.

In Fig. 8 we also show, for comparison, the counts in total flux density at 100 GHz given by the De Zotti et al. (2005) model ('D05', indicated by the thick blue line). The C2Ex model is displayed as a thick violet line. The observed counts are from the South Pole Telescope (SPT; Mocanu et al. 2013) and from *Planck* (Planck Collaboration XIII 2011). In polarization we also plot the 'optimistic' prediction for polarized source counts by Tucci & Toffolatti (2012) as a thin violet line and the convolution of the D05 model with our distribution for the polarization fraction (at 97.5 GHz) as thin blue line. Since the latter model tends to overestimate the source counts at such high frequency, we can assume the associated line as a 'pessimistic' prediction. On the contrary, as displayed in Fig. 8, there is a very remarkable agreement between our current data and the model predictions by Tucci & Toffolatti (2012).

6 PECULIAR OBJECTS

Fig. 9 shows, from left to right, the Stokes I, Q, and U images for the first 4 sources, ordered in RA. Whenever the source was detected both in Q and in U, we have superimposed to the I image a vector showing the direction of linear polarization.

All the objects in the sample were selected as being point-like at 20 GHz but some of them are spatially resolved by ALMA. Sources AT20GJ040820−654508, AT20GJ050644−610941, AT20GJ063546−751616, AT20GJ074331−672625, and AT20GJ080633−711217 seem to display jet components displaced from the central core. However, such components are at least two orders of magnitude fainter than the core (see images similar to Fig. 9 provided as supplementary online material); hence, for the purposes of this paper, these sources are effectively point-like.

Instead AT20GJ040848−750720 and the leakage calibrator, PKS0521−365 (which, however, does not belong to the sample), are well resolved by ALMA and show a peculiar structure in polarization. Therefore they deserve more discussion.

AT20GJ040848−750720

This is an FR-II source at $z \simeq 0.69$. It was unresolved by ATCA at 20 GHz, although the centroid in polarization was slightly offset from that in total intensity. The ALMA image (with 0.5 arcsec resolution) shows that the emission is dominated by two bright lobes (cf. Fig. 10). Both exhibit a high depolarization, slightly higher in the eastern one. The latter also shows a double structure in the polarized emission. The core sits mid-way of the two lobes and is quite faint, i.e. $\simeq 1.5$ mJy (cf. Fig. 10).
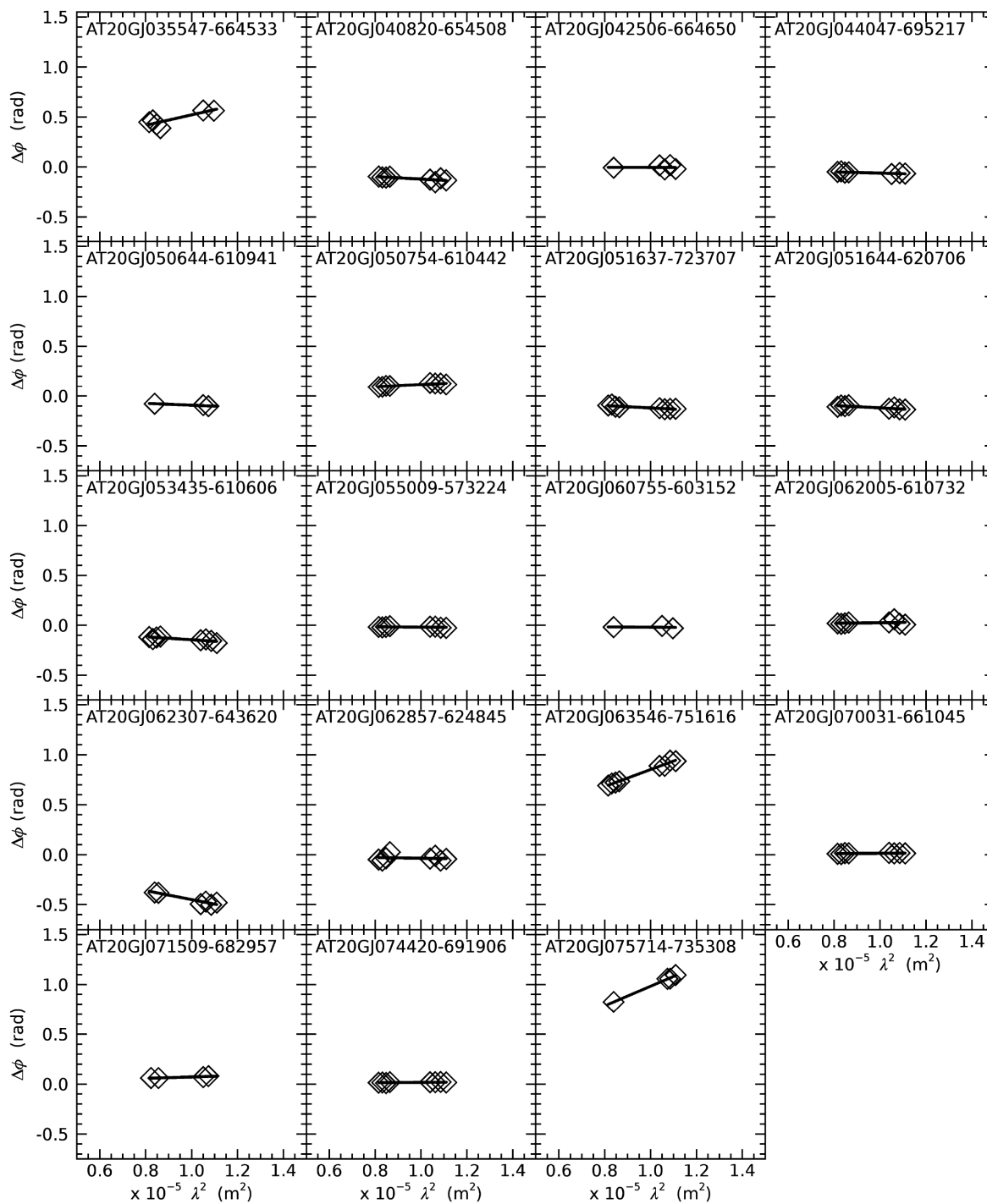
Figure 7. Successful RM fits for 19 objects of the complete sample observed with ALMA between 90 and 105 GHz.

PKS0521−365

This nearby ($z = 0.0554$) radio-loud object is a bright γ-ray source and exhibits a variety of nuclear and extranuclear phenomena (Falomo et al. 2009). It is one of the most remarkable objects in the southern sky: it is one of the three known BL Lac objects showing a kiloparsec-scale jet well resolved at all bands (Liuzzo et al. 2011). The ALMA image (Fig. 11) shows a one-sided radio jet extending in the N-W direction up to 7 arcsec from the nucleus. The jet exhibits many knots, also detected from the optical to X-

rays (Falomo et al. 2009). A hotspot located at 8 arcsec from the nucleus in the south-east direction is also detected in all bands. At low frequency, the arcsecond-scale radio structure is dominated by an extended lobe. The overall energy distribution of PKS0521−365 is consistent with a jet oriented at about 30° with respect to the line of sight. This is also in agreement with the absence of superluminal motion in the parsec-scale jet (Falomo et al. 2009). In the millimetre bands, extended structures (hotspot and jet) of this object are detected up to 320 GHz; their morphology is similar to that

Table 5. List of the 11 objects with an observed RM in ALMA Band 3 (90–105 GHz) non-compatible with a null rotation at a 1σ level. We also report for each source the corresponding RMs found at lower frequencies (if any), the inferred number of synchrotron components and the redshift, when available (provided by Galluzzi et al. 2018). RMs and associated errors are in rad m^{-2}.

(AT20G) name	RM$_{obs}$			σ_{RM}	# Comp	z
	2–9	18–38	90–105	90–105 GHz		
J035547−664533	−12	–	52 075	13 673	>3	0.73
J044047−695217	–	1500	−6243	2550	2	–
J050644−610941	–	–	−9305	7992	2	1.09
J050754−610442	–	400	11 593	10 427	2	1.09
J051637−723707	−21	−3200	−12 039	10 037	2	–
J051644−620706	54	200	−11 976	10 482	3	1.30
J053435−610606	–	0	−14 498	8696	>3	2.00
j062307−643620	78	–	−44 998	5792	2	0.13
J063546−751616	16	−800	85 187	7860	2	0.40
J071509−682957	–	700	7131	5381	2	–
J075714−735308	–	–	98 273	10 877	2	–

Table 6. Median values of the RMs between 90 and 105 GHz. The upper part of the table refers to the observed RMs for the 11 sources with a non-null value at 1σ level. The lower part gives the RMs at the source for the subset of objects for which redshift measurements are available. In parenthesis are the numbers of objects in each group. RMs are in rad m^{-2}.

All sample (11)	2–3C (9)	>3C (2)
1.2×10^4	1.2×10^4	3.3×10^4
All sample (7)	2–3C (5)	>3C (2)
6.4×10^4	5.7×10^4	1.4×10^5

Table 7. Euclidean normalized differential source counts at 95 GHz in polarized flux density given by equation (5).

log [$P(Jy)$]	$P^{5/2}n(P)$ (Jy$^{3/2}$sr^{-1})	Lower error	Upper error
−2.920	0.0263	0.0106	0.0106
−2.759	0.0308	0.0124	0.0124
−2.598	0.0362	0.0145	0.0145
−2.437	0.0427	0.0169	0.0169
−2.276	0.0504	0.0198	0.0198
−2.115	0.0594	0.0234	0.0234
−1.955	0.0699	0.0278	0.0278
−1.794	0.0817	0.0334	0.0334
−1.633	0.0944	0.0402	0.0402
−1.472	0.1075	0.0485	0.0485
−1.311	0.1201	0.0583	0.0583
−1.151	0.1313	0.0694	0.0694
−0.990	0.1401	0.0818	0.0851
−0.829	0.1456	0.0951	0.1021
−0.668	0.1472	0.1088	0.1236
−0.507	0.1442	0.1226	0.1544
−0.346	0.1359	0.1324	0.1997
−0.186	0.1214	0.1386	0.2798
−0.025	0.1007	0.1911	0.4645
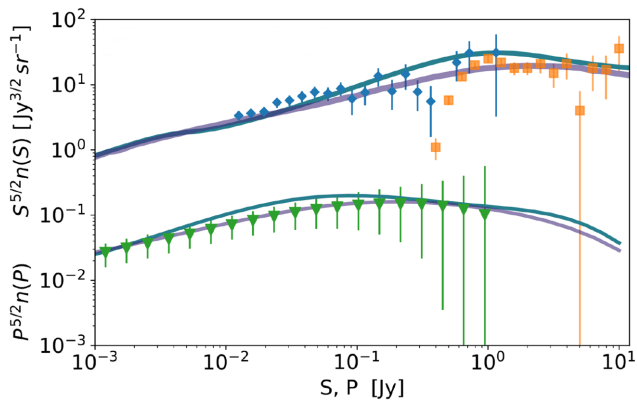
Figure 8. Euclidean normalized differential number counts at 95 GHz. The blue lines represent the number counts as predicted by De Zotti et al. (2005, D05) model in total intensity (thicker upper line) and in polarization (once convolved with our histogram of the polarization fraction, see the thinner lower line). The C2Ex model in total intensity and relative 'optimistic' prediction in polarization presented by Tucci & Toffolatti (2012) is shown as violet lines (the thick and the thin ones, respectively). The observed total intensity source counts from SPT (blue diamonds; Mocanu et al. 2013) and from *Planck* (orange squares; Planck Collaboration XIII 2011) are also plotted. Our differential number counts in the polarized flux density computed via equation (5) are shown by green triangles.

observed from the optical to X-rays (Liuzzo et al. 2015; Leon et al. 2016).

Polarimetric data for such resolved objects are very helpful to perform studies aimed at addressing fundamental questions about the AGN physics, such as the role of the magnetic field in jetted/radio loud AGNs, the plasma properties and particle acceleration mechanisms. By using more advanced techniques, such as the Faraday Rotation Measure Synthesis (Brentjens & de Bruyn 2005) or procedures similar to those adopted by O'Sullivan et al. (2012), it is possible to obtain a 3D representation of the magnetic field. A paper from our collaboration (Liuzzo et al., in preparation) will exploit such techniques on PKS0521−365 maps, trying, among other things, to address the physical processes operating in the hotspots (e.g. Fermi-II acceleration or multiple shocks, cf. Prieto, Brunetti & Mack 2002).

6.1 Calibrator candidates for CPR studies

As briefly discussed in the Section 1, the CPR studies, which rely on the statistical analysis of a collection of objects, typically suffer from the lack of zero-point calibration of the polarization angle. Thus, having reference objects whose polarization angle is known on a sub-degree scale is particularly helpful for those
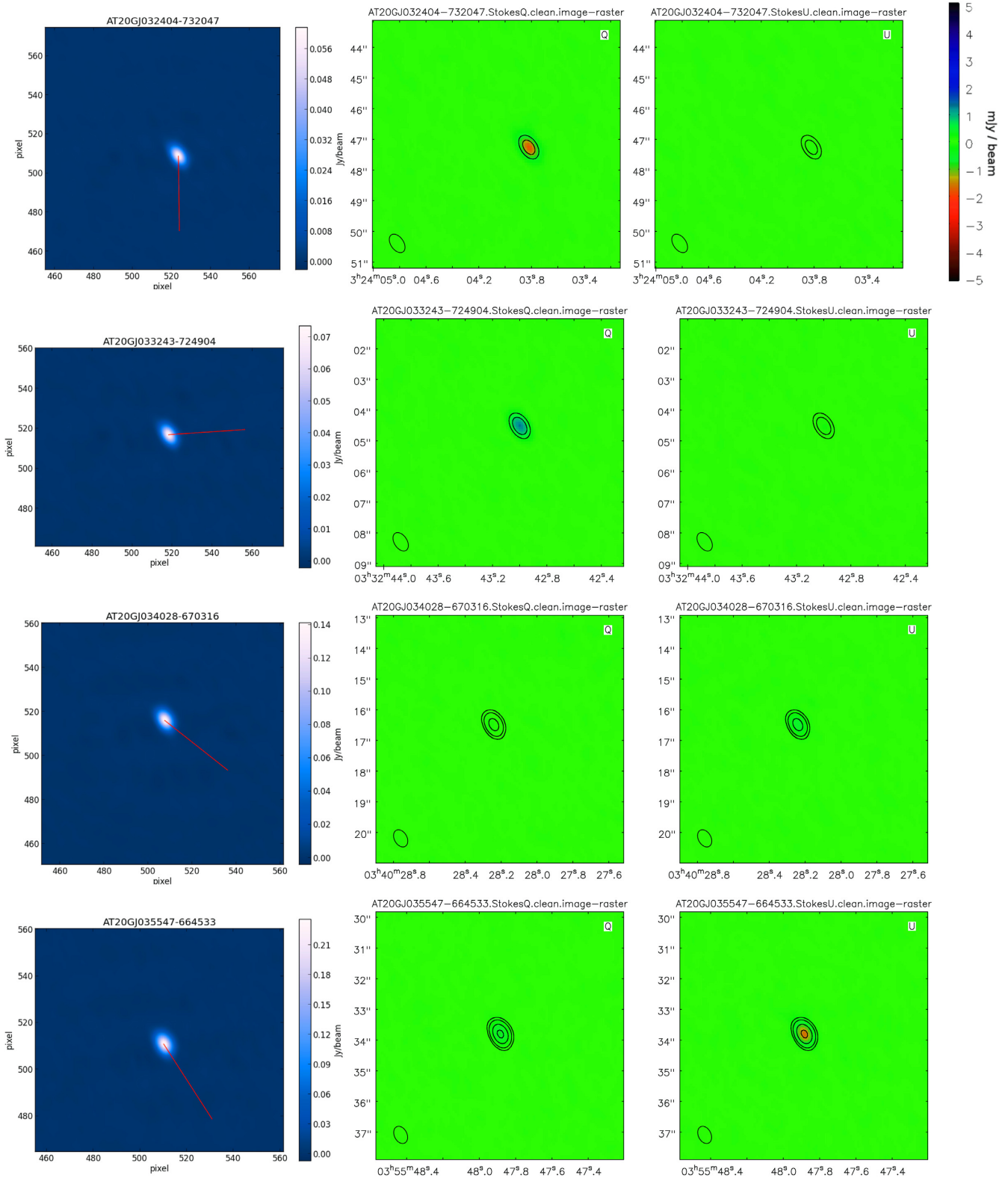
Figure 9. Stokes *I*, *Q*, and *U* images of the first 4 objects (ordered by RA) observed with ALMA. We have superimposed to each *I* map polarization vectors indicating the polarization angle, by using the Key analysis Automated FITS-Image Explorer (KAFE; Burkutean et al. 2018) package. For *Q* and *U* maps we use the same data range (displayed by the colour wedge attached to the first U map). We also overplot total intensity maps by contours with levels at 20, 50, 100, 200, 500, and 1000 mJy. The images for the other objects are provided online as supplementary material.
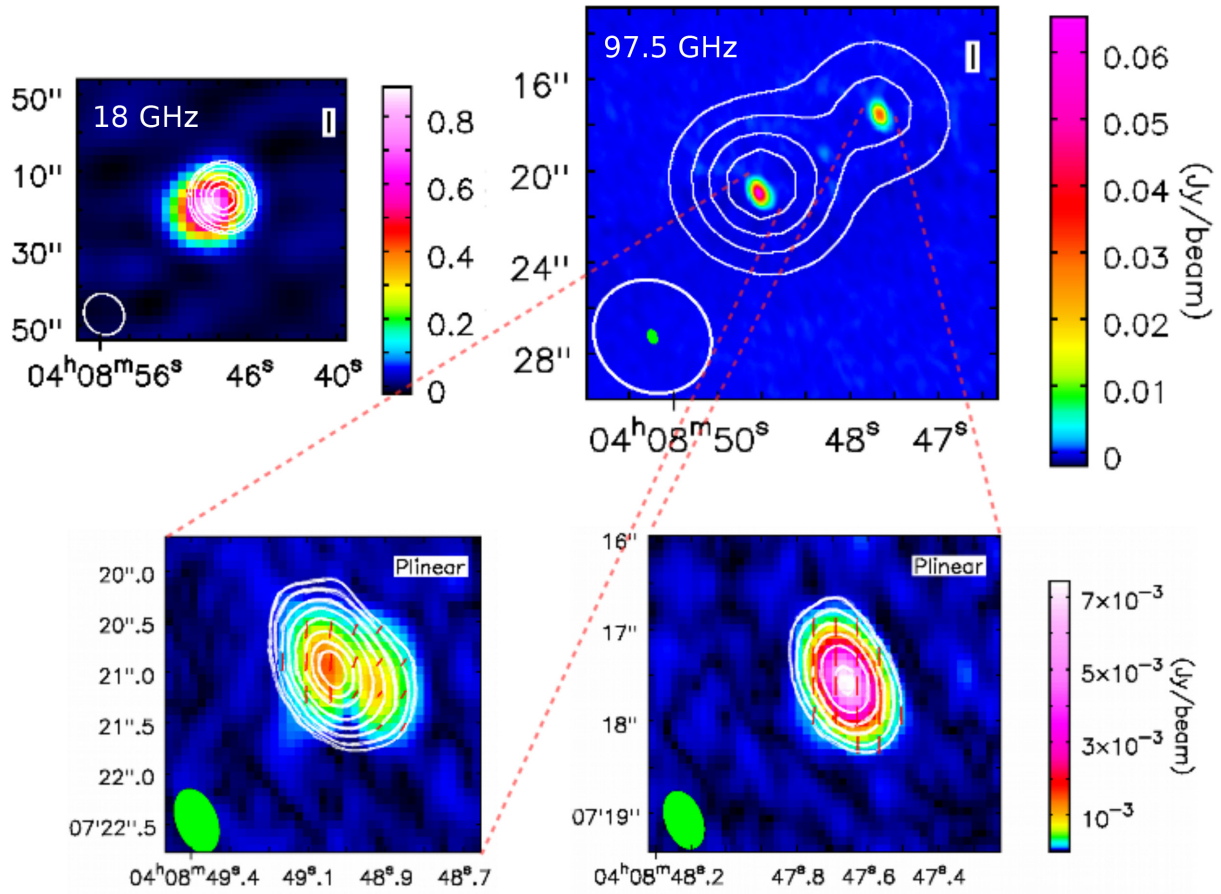
Figure 10. Images of AT20GJ040848−750720. The upper-left panel shows the ATCA image at 18 GHz, where the white contours refer to polarization, the other multicolour contours refer to total intensity. The upper-right panel shows the total intensity ALMA image at 97.5 GHz (multicolour contours) together with total intensity contours (more extended lines) from the ATCA image at 38 GHz. In the bottom left corner of each panel we display the ATCA (white contour) and ALMA (green filled ellipse) synthesized beams. The lower panels show the ALMA polarization image (multicolour) and total intensity (white) contours with superimposed the magnetic field directions (in red) for the eastern and the western hotspots (left-hand and right-hand panel, respectively).
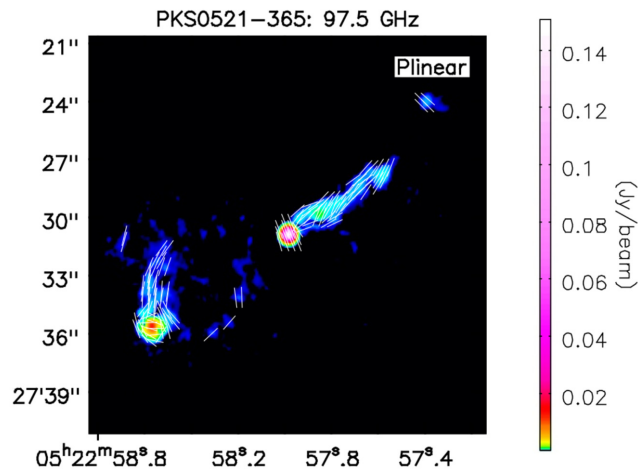
Figure 11. Linearly polarized emission (multicolour contours) and position angles (vectors) in ALMA Band 3 of PKS0521−365.

studies: good candidates might be compact radio sources which show bright total flux densities (at least of few hundreds of mJy), with a polarization fraction at least of a few per cent and a reasonably stable behaviour in the polarization angle. Until now,

the essential lack of polarimetric observations at high frequencies and consequent monitoring on large samples of radio sources make these calibrators very rare, especially in the southern sky.

Both our ALMA and ATCA polarization angle measurements are free from the zero-point systematic error arising from the phase difference in the cross-correlation products of the reference antenna. In the case of ATCA each antenna receiver at the frequencies we observed is equipped with a noise diode mounted in one of the linear feeds. The signal injected by each diode is received by the other feed and phase differences are characterized for all the antennas and stored in visibility files. During the data reduction with MIRIAD (the standard radio interferometry package for ATCA) a reference antenna is set and the relative phase difference correction is applied to the data. In the case of ALMA, the determination of this systematic term can be achieved by observing a polarized object at different parallactic angles for a typical angular coverage of at least 3 h, in order to break degeneracies associated with the unknown polarization signal of the calibrator itself and leakage terms. Thus, we searched in our sample (up to 105.5 GHz) sources suitable as CPR calibrators.

We firstly restricted ourselves to those found to be the less variable ones in both total intensity and polarization (typically less than 10 per cent) and which are also stable in the polarization angle at the different epochs we observed. Then, we selected those

with relatively high-flux densities (at least 100 mJy at 97.5 GHz) and polarization fractions (especially at frequencies higher than 20 GHz) at least at a few per cent level. The first object we selected is PKS0637−752 (also known as AT20GJ063546−751616), already suggested by Massardi et al. (2013) as a potential leakage calibrator, being at ∼ 1 Jy and ∼ 1.6 per cent polarized at 97.5 GHz. Our ATCA observations show that the polarization angle is quite constant across the 5.5–38 GHz frequency range and stable within $8°$ at 38 GHz between 2014 September and 2016 July (see Fig. 2). However, this object displays FR in different frequency regimes (see Table 5): at ALMA frequencies, between 90 and 105 GHz the polarization angle absolute variation is $\simeq 14°$. Other somewhat fainter but more polarized objects we found in our sample are AT20GJ062005−610732 (120 mJy, 10.5 per cent polarized) and AT20GJ074331−672625 (190 mJy, 5.2 per cent polarized): the first one is constant within $8°$ both across the 18–38 GHz frequency range and between the two epochs; the second is less constant between the different frequencies but stable within $\sim 3°$ both at 33 and 38 GHz.

The objects we have identified are potential calibrators for CPR studies: the fact their variability in the polarization angle is no more than $8°$, over a period of almost 2 yr, might indicate a stability at sub-degree level over a period of (at least) few days. The latter is the main requirement to reduce systematics in CPR experiments as well as for CMB studies. We are going to monitor on a more regular basis these objects both with ATCA and with ALMA at higher frequencies (Band 3 and 6, i.e. 97.5 and 243 GHz, respectively).

7 CONCLUSIONS

We have presented and discussed high sensitivity ALMA polarimetric observations in Band 3 (97.5 GHz) of a complete sample of 32 extragalactic radio sources (in the region with $b < -75°$) drawn from the faint PACO sample, i.e. compact AT20G sources with $S_{20GHz} \geq 200$ mJy. The rms in polarized flux density was 0.4 mJy, which allowed a detection rate of 94 per cent at 5σ.

ALMA observations (together with ATCA and GLEAM data) allowed us to reach more than 3 decades of spectral coverage in total intensity and ∼1.7 decades in polarization. Most of the sources (26 out of 32) revealed a flux density excess in total intensity with respect to spectra extrapolated from ATCA data at lower frequencies (collected between 2 and 6 months before ALMA measurements), suggesting the emergence of another emission component. The high frequency emissions are polarized at a few per cent level. None of the observed spectra showed signs of any synchrotron break, and the spectral indices in total intensity between 36.5 and 97.5 GHz are typically flat, i.e. $\simeq -0.19$. The distribution of polarization fractions observed with ALMA allowed us to extend the analysis of Galluzzi et al. (2018) up to 97.5 GHz, confirming the absence of any statistically significant trend with the frequency (or the flux density). This data set has been included in the analysis described in Puglisi et al. (2018), which presents the state-of-the-art about polarimetry of extragalactic radio sources and provides forecasts for their contamination of the B-mode angular power spectrum, useful for current and forthcoming CMB experiments. Besides, our observed polarization fractions further confirm the results obtained from Planck maps by Bonavera et al. (2017, adopting a stacking technique) and by Trombetti et al. (2018, exploiting IDA method).

We also looked for differences in the high frequency polarization properties of different sub-classes of sources, using classifications based on spectral indices or on the number of components detected

in source spectra, but the smallness of the sample prevented any firm conclusion.

By exploiting the 8 GHz ALMA bandwidth, we investigated the RMs at ∼ 100 GHz. We found intrinsic values $\simeq 6.4 \times 10^4$ rad m^{-2}, at least one order of magnitude higher than those obtained for the 18–38 GHz frequency range and two orders of magnitude higher than in the 2–9 GHz range. Although with large uncertainties, these results suggest the presence of dense screens of magnetized plasma that can strongly depolarize the mm-wave emission, suppressing the increase in the polarization fraction due to more ordered magnetic fields, typically expected in the regions of the jet closer to the nucleus.

We have also presented estimates of source counts in linearly polarized flux density at 95 GHz, derived from the convolution of the model C2Ex by Tucci et al. (2011) for total intensity source counts with the distribution of polarization fractions for our sample.

Two objects in our data set, namely the target AT20GJ040848−750720 and the calibrator PKS0521−365, show well-resolved structures, which constitute interesting case studies to constraint magnetic fields and particle acceleration mechanisms along AGN jets and in hotspots: a preliminary description of these sources has been presented here. However, a more exhaustive investigation will be addressed by future publications (e.g. Liuzzo et al., in preparation) as well as by further observations. In fact, maps obtained for PKS0521−365 show that ALMA, with an angular resolution ∼ 0.2 arcsec, can reveal polarized emission even in the lobes, by spending only 10 min on source. This demonstrates the power of ALMA in detecting faint (< 0.1 mJy) source components for large samples of sources.

Finally, by considering the less variable but (at the same time) the brightest and the most polarized objects in our sample, we have identified three cases that display particular stability in the polarization angle, both in time and frequency (especially at higher frequencies). These (as well as similar) objects may serve as polarization angle calibrators for improving future CPR studies, by reducing the currently limiting calibration error below the degree level.

REFERENCES

Ackermann M. et al., 2015, ApJ, 810, 14A

Agudo I., Thum C., Gómez J. L., Wiesemeyer H., 2014, A&A, 566, A59

Arkin H., Colton R. R., 1970, Statistical methods, 5th edn., Barnes & Noble, New York

Bonavera L., Gonzáles-Nuevo J., Argüeso F., Toffolatti L., 2017, MNRAS, 469, 2401

Böttcher M., 2012, preprint (arXiv:1205.0539)

Brentjens M. A., de Bruyn A. G., 2005, A&A, 441, 1217

Burkutean S. et al., 2018, J. Astron. Telesc. Instrum. Syst., 4, 028001

Cutini S. et al., 2014, MNRAS, 445, 4316

De Zotti G., Ricci R., Mesa D., Silva L., Mazzotta P., Toffolatti L., González-Nuevo J., 2005, A&A, 431, 893

di Serego Alighieri S., 2015, Int. J. Mod. Phys. D, 24, 1530016

Falomo R. et al., 2009, A&A, 501, 907

Fromm C. M., Fuhrmann L., Perucho M., 2015, A&A, 580, A94

Fuhrmann L. et al., 2016, A&A, 596, A45

Galluzzi V. et al., 2017, MNRAS, 465, 4085

Galluzzi V. et al., 2018, MNRAS, 475, 1306

Gehrels N., 1986, ApJ, 303, 336

Hovatta T., O'Sullivan S., Martí-Vidal I., Savolainen T., Tchekhovskoy A., 2019, A&A, 623, A111

Hughes P. A., Aller H. D., Aller M. F., 1985, ApJ, 298, 301

Hughes P. A., Aller H. D., Aller M. F., 1989, ApJ, 341, 54

Hurley-Walker N. et al., 2017, MNRAS, 464, 1146

Jorstad S. G. et al., 2013, ApJ, 773, 147

Jorstad S. G. et al., 2007, AJ, 134, 799

Leon S., Cortes P. C., Guerard M., Villard E., Ocanã F. B., Vila-Vilaro B., 2016, A&A, 586, A70

León-Tavares J., Valtaoja E., Tornikoski M., Lähteenmäki A., Nieppola E., 2011, A&A, 532, A146

Liuzzo E., Falomo R., Treves A., 2011, preprint (arXiv:astro-ph/1105.5226)

Liuzzo E., Nagai H., Giovannini G., Mignano A., 2015, ASP Conf. Ser. Vol. 499, Revolution in Astronomy with ALMA: The Third Year. Astron. Soc. Pac., San Francisco, p. 129

Marscher A. P., 1996 , ASP Conf. Ser. Vol. 100, Energy Transport in Radio Galaxies and Quasars. Astron. Soc. Pac., San Francisco, p. 45

Marscher A. P., Gear W. K., 1985, ApJ, 298, 114

Massardi M., Bonaldi A., Bonavera L., López-Caniego M., De Zotti G., Ekers R. D., 2011, MNRAS, 415, 1597

Massardi M. et al., 2013, MNRAS, 436, 2915

Massardi M., Bonaldi A., Bonavera L., De Zotti G., López-Caniego M., Galluzzi V., 2016, MNRAS, 455, 3249

Mauch T., Murphy T., Buttery H. J., Curran J., Hunstead R. W., Piestrzynski B., Robertson J. G., Sadler E. M., 2003, MNRAS, 342, 1117

Mocanu L. M. et al., 2013, ApJ, 779, 61

Nagai H. et al., 2016, ApJ, 824, 132

Ni W. T., 2010, Rep. Prog. Phys., 73, 056901

O'Sullivan S. P. et al., 2012, MNRAS, 421, 3300

Planck Collaboration XIII, 2011, A&A, 536, A13

Planck Collaboration XV, 2011, A&A, 536, A15

Prieto M. A., Brunetti G., Mack K. H., 2002, Science, 298, 193

Puglisi G. et al., 2018, ApJ, 858, 85

Ramakrishnan V. et al., 2016, MNRAS, 456, 171

Remazeilles M. et al., 2018, J. Cosmol. Astropart. Phys., 2018, 023

Trombetti T., Burigana C., De Zotti G., Galluzzi V., Massardi M., 2018, A&A, 618, A29

Tucci M., Toffolatti L., 2012, Adv. Astron., 2012, 624987

Tucci M., Toffolatti L., De Zotti G., Martínez-González E., 2011, A&A, 533, A57

SUPPORTING INFORMATION

Supplementary data are available at *MNRAS* online.

IQU_Images_Supplementary_Material_resubmission.pdf
ALMA_Catalogue_resubmission.txt

Please note: Oxford University Press is not responsible for the content or functionality of any supporting materials supplied by the authors. Any queries (other than missing material) should be directed to the corresponding author for the article.

This paper has been typeset from a TEX/LATEX file prepared by the author.